nature

SUPPLEMENTARY INFORMATION

https://doi.org/10.1038/s41586-019-0971-3

In the format provided by the authors and unedited.

Random anti-lasing through coherent perfect absorption in a disordered medium

Kevin Pichler[1], Matthias Kühmayer[1], Julian Böhm[2], Andre Brandstötter[1], Philipp Ambichl[1], Ulrich Kuhl[2,3]* & Stefan Rotter[1,3]*

[1]Institute for Theoretical Physics, Vienna University of Technology (TU Wien), Vienna, Austria. [2]Institut de Physique de Nice, Université Côte d'Azur, CNRS, Nice, France. [3]These authors jointly supervised this work: Ulrich Kuhl, Stefan Rotter. *e-mail: ulrich.kuhl@unice.fr; stefan.rotter@tuwien.ac.at

Supplementary information

Random anti-lasing through coherent perfect absorption in a disordered medium

Kevin Pichler[1], Matthias Kühmayer[1], Julian Böhm[2], Andre Brandstötter[1], Philipp Ambichl[1], Ulrich Kuhl[2], and Stefan Rotter[1]

Affiliations:

[1] Institute for Theoretical Physics, Vienna University of Technology (TU Wien), A-1040 Vienna, Austria, EU

[2] Institut de Physique de Nice, Université Côte d'Azur, CNRS, F-06100 Nice, France, EU

Supplementary section 1 – Injection of specific states

A major requirement for the realisation of a coherent perfect absorber (CPA) is the ability to inject suitably shaped input states into the system – in our case S-matrix eigenstates with vanishing eigenvalue. In this respect it is essential that desired input states can be accurately generated following the protocol explained in the methods section of the main manuscript. Here we test this protocol by applying it to an empty waveguide (i.e. without the disordered medium) with the goal to inject the four transverse modes supported in the investigated frequency range between 6 GHz and 7.5 GHz. The resulting microwave field has been measured about 20 cm away from the injection antennas and the results are presented in Fig. S1. The microwave field measured over the waveguide width for each of the injected transverse modes (Fig. S1a) clearly shows the expected mode shapes. Small deviations from the perfect form are the result of reflections due to unavoidable experimental imperfections in the system. Moreover, the analysis of the measured signal in the mode domain (Fig. S1b) yields the expected mode composition for all measurements and proves the functionality of our injection method.

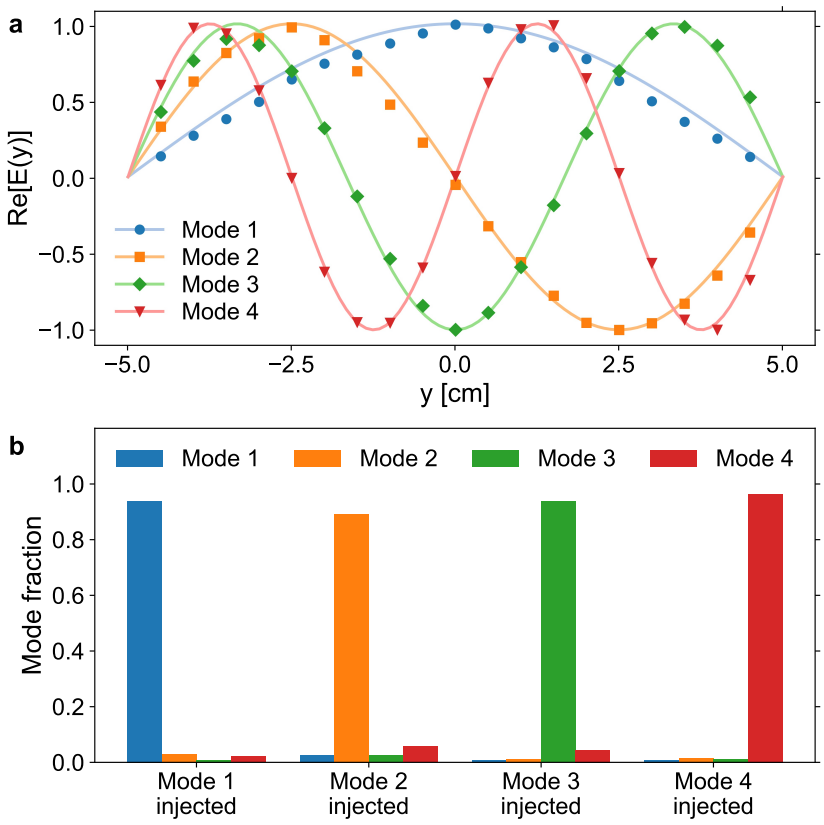

Supplementary figure S1: Injection accuracy analysis of specific states. a, Injection of the four possible transverse modes from one side into the empty waveguide (without the central antenna or any other obstacles placed in the waveguide). The solid curves describe the expected mode shape and the markers show the normalised measured field values E over the waveguide width (y-direction) for each of the injected modes. **b,** Analysis of the injected signals from **a** in the mode domain. The bars illustrate the fraction of the respective mode in the incoming signal into the waveguide.

Supplementary section 2 – Determination of the scattering matrix

Our approach to realise a CPA requires the measurement of the scattering matrix (S-matrix) of the system and to search for vanishing eigenvalues in order to inject the corresponding eigenstates into the system. The S-matrix connects the outgoing waves with the injected signals in a linear manner,

$$\boldsymbol{a}_{\mathrm{out}} = S\,\boldsymbol{a}_{\mathrm{in}} = \begin{pmatrix} R_{\mathrm{L}} & T_{\mathrm{R}} \\ T_{\mathrm{L}} & R_{\mathrm{R}} \end{pmatrix} \boldsymbol{a}_{\mathrm{in}},$$

where T_{L} and T_{R} are the transmission sub-matrices and R_{L} and R_{R} are the reflection sub-matrices, respectively, with regard to the modes on the left and right side of the waveguide, indicated by the subscripts L and R. As a benchmark we have determined the S-matrix of an empty waveguide (i.e. without disordered medium) with the procedure described in the methods section of the manuscript. The results, illustrated in Fig. S2 (left), show the diagonal form of the quadratic transmission matrix blocks in the S-matrix of the empty waveguide (the elements in the quadratic reflection matrix blocks are all strongly reduced). This is the result expected for an empty waveguide without scattering or back-reflection featuring only a length-dependent scattering phase shift in transmission together with a small attenuation due to absorption in the metallic waveguide material. The minor deviations from this ideal picture are attributed to experimental imperfections as well as to the presence of the eight weakly coupled external antennas that were left in place for this measurement.

The situation changes when scattering objects are embedded in the system. In this case, the mode compositions of the incoming and outgoing signals become different, which is illustrated by a non-diagonal transmission matrix and non-zero reflection

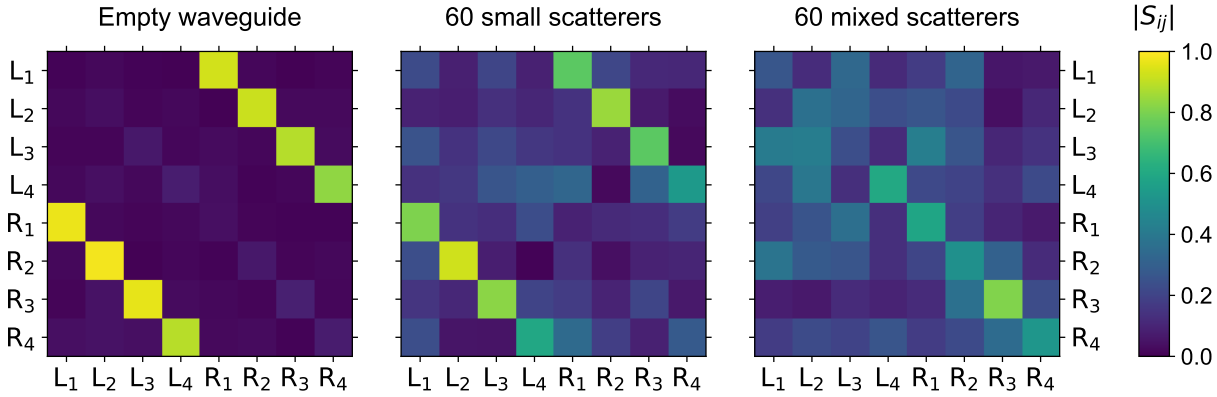

Supplementary figure S2: Typical scattering matrices for different scatterer configurations. (Left panel) For the empty waveguide (without disordered medium), the scattering matrix (S-matrix) is close to diagonal in the transmission sub-matrices (top right and bottom left 4×4 sub-matrices) and close to zero in the reflection sub-matrices (top left and bottom right 4×4 sub-matrices). The labels denote the left (L_n) and right (R_n) side of the waveguide, where the subscript represents the respective mode number. (Middle panel) For the system shown in Figs. 1 and 2 of the main text with 60 small scatterers (radius 2.55 mm), the S-matrix gets occupied all over its 8x8 entries with the diagonal elements of the transmission sub-matrices remaining more pronounced than the remaining S-matrix elements. (Right panel) For the system shown, among others, in Figs. 3 and 4 of the main text featuring 60 scatterers of mixed sizes (radii 2.55 mm and 11 mm), the S-matrix is more uniformly occupied. The S-matrices for the empty waveguide and for the configuration with 60 small scatterers were evaluated at a frequency of $\upsilon = 7.1$ GHz, and for the configuration with 60 mixed size scatterers at a frequency of $\upsilon = 6.9$ GHz.

matrix elements, as can be seen in Fig. S2 (centre) for our system with 60 small scatterers (radius 2.55 mm). With increasing scattering strength, which is influenced by the number and sizes of the scatterers in the system, the S-matrix gets more and more off-diagonal. This can be nicely seen in Fig. S2 (right), where we show the S-matrix of our system with 60 scatterers of mixed sizes (radii 2.55 mm and 11 mm), that scatter incoming waves more strongly than the configuration with equal-size scatterers. In section 8 we investigate how these different scattering strengths can be characterised by appropriate mean free paths.

Supplementary section 3 – Central antenna coupling

One crucial ingredient for realising a CPA in our experiment is the proper absorption strength of the local absorber, which is realised by a monopole antenna in our experiment. In order to characterise the properties of this antenna, we determine the antenna coupling for different antenna lengths L, measured from the lower boundary of the top plate to the antenna end (see sketch in Fig. S3.1a). For each length value we determine the reflection incurred for emission into the open half space below the top plate of the waveguide. In Fig. S3.1b we investigate the reflection signal $|R|^2$ in a broad frequency range from 1 GHz to 20 GHz. We observe a resonant behaviour of all the antennas with different length in the sense that the reflection signal shows a minimum that shifts in its spectral position with the antenna length, but that always occurs above 7.5 GHz. The inset in Fig. S3.1b shows a zoom into the relevant frequency region considered in our experiments (6.55 GHz to 7.35 GHz). We see very clearly that the antenna coupling is generally increasing with the antenna length (as expected) and that the frequency-dependence for each specific antenna length remains flat (without any resonant features etc.). We may thus safely conclude that the CPA points and the associated critical coupling conditions that we discuss in the main text are not due to an intrinsic property of the antenna itself.

In a next step we characterise the absorption of the central antenna in the empty waveguide (without any scatterers). A meaningful estimate of the antenna's

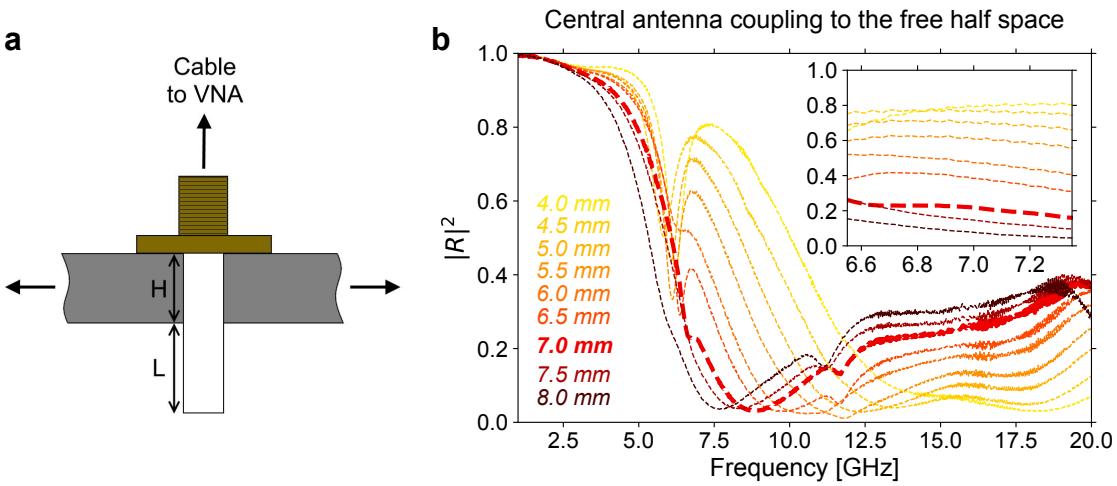

Supplementary figure S3.1: Central antenna coupling to the free half-space. a, Illustration of the position of the central antenna in the top plate of the waveguide and its connection to the vector network analyser (VNA). The length L of the antenna's extension below the top plate is given by the difference between the total antenna length and the height of the top plate H. **b,** Reflection coefficient $|R|^2$ for the configuration in **a** measured for different lengths L.

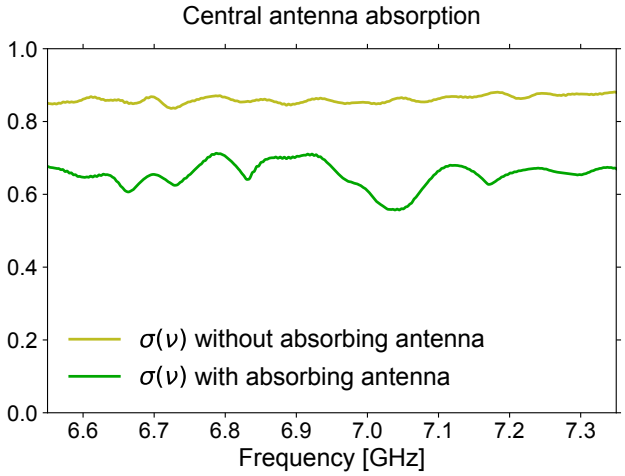

Supplementary figure S3.2: Central antenna coupling to the empty waveguide. Average scattering matrix eigenvalue of the empty waveguide, $\sigma(\upsilon) = (\sum_{n=1}^{8}|\lambda_n|^2)/8$, in the absence and presence of the absorbing antenna positioned as in Fig. 2 of the main text (length 7 mm).

absorption cross section can be extracted from a measurement of the scattering matrix with and without the antenna present in the empty waveguide. Specifically we evaluate (for the waveguide without scatterers) the average at a given frequency υ over all scattering matrix eigenvalues λ_n (in their absolute values squared), $\sigma(\upsilon) = (\sum_{n=1}^{8}|\lambda_n|^2)/8$, for the two cases with and without the central antenna present. The corresponding quantity σ and its dependence on the frequency υ within the spectral interval we work in is depicted in Fig. S3.2 for the antenna used in Fig. 2 of the main text (with a length of 7 mm) and without it. In this plot we notice that the presence of the antenna leads to a considerable reduction of the intensity that leaves the waveguide again after being injected. Moreover, the antenna also gives rise to more pronounced variations in $\sigma(\upsilon)$ (as compared to those observed for the empty waveguide). Since these variations are not an intrinsic feature of the antenna (see above discussion), they are probably due to the scattering between the antenna and the confinement (in y-direction) by the waveguide walls, which naturally features some dispersion. These variations are, however, rather weak in their magnitude ($\sigma(\upsilon)$ always stays in the interval [0.55,0.72]) and the minima in $\sigma(\upsilon)$ notably do not coincide with any of the CPA positions we identify in the main text. Averaged over the frequency interval from 6.55 GHz and 7.35 GHz, we find that the antenna reduces the corresponding mean value $\langle\sigma(\upsilon)\rangle_\upsilon$ by 24.0%. We mention here that reflection measurements as in Fig. S3.1b are considerably less time consuming than scattering matrix measurements as in Fig. S3.2, for which reason we studied only one antenna length in the latter case.

Supplementary section 4 – Simulation of the microwave field

As described in the methods section of the main manuscript, we simulate the microwave field in the waveguide by solving a two-dimensional scalar Helmholtz equation for transverse-electric modes. Experimentally, we measure the wave function on a 5×5 mm grid around the absorbing antenna allowing us to compute the correlation between the intensity profiles of the experimentally measured and numerically calculated CPA state. For a meaningful comparison we also map the numerical results that we obtain with very high spatial resolution to the same reduced 5×5 mm grid as in the experiment. Since the electric field cannot be measured in the

close vicinity of the central antenna or inside the scatterers, we also exclude the corresponding points from these pixelated data sets. A comparison of the experimental and pixelated numerical intensity profiles is shown in Fig. S4. For the configuration with 60 small scatterers (see Fig. S4a) we find a correlation of 95.63%, whereas the correlation in the configuration with 60 scatterers of mixed sizes (see Fig. S4b) is 83.42%. We attribute the deviations from the perfect correlation value (100%) to the uncertainty of about 1 mm in the experimentally realised position of each scatterer as compared to the values used for the simulations. Since the strongly scattering system with mixed scatterers is more sensitive to such deviations, this also explains why the correlation value is lower here than for the case of weak scattering. Another source for reduced correlations are the unavoidable experimental imperfections that are not taken into account in the simulations. One specific aspect we neglected in our simulations is the global absorption in the waveguide. When taking global absorption into account (following Ref. [30] in the manuscript) based on material parameters for our waveguide made of aluminium, the intensity correlation values for the two CPA states from above stay unchanged on the percent level. Specifically, the correlation values for the configuration with 60 small and 60 mixed scatterers are then 95.57% and 83.44%, respectively. The reason why global absorption has a weak effect on the CPA states we discuss in the main text is because for these states the loss incurred at the central antenna is much more dominant than the weak dissipation in the waveguide.

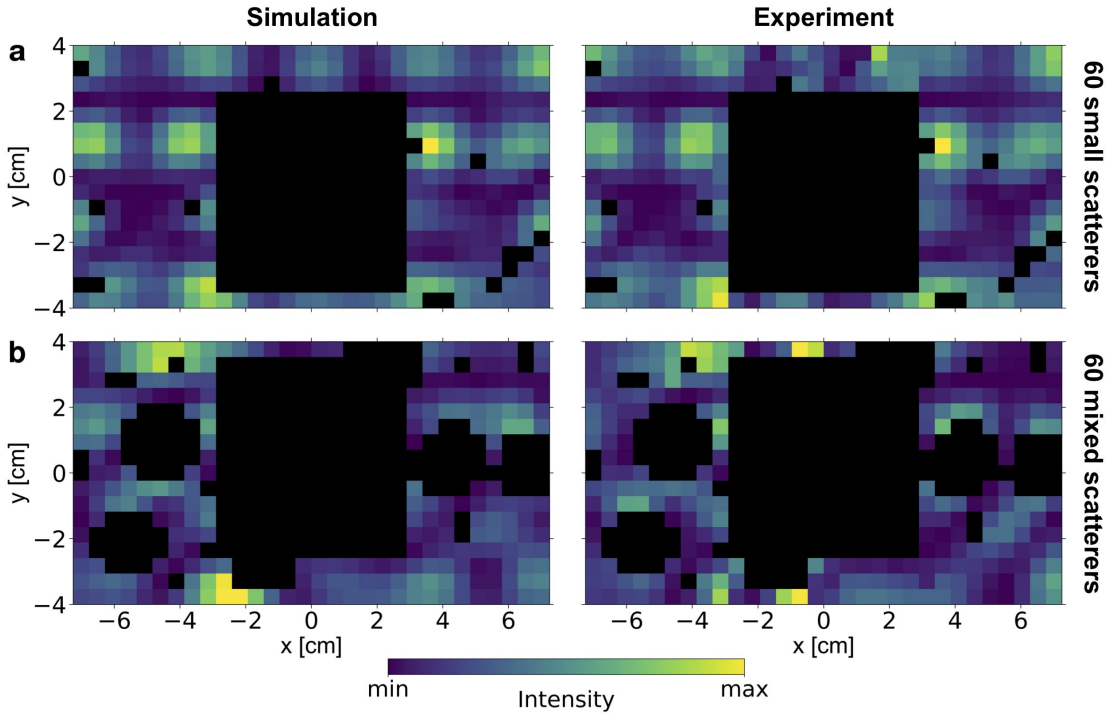

Supplementary figure S4: Microwave intensity around the central antenna for CPA states. a, Comparison between simulated and measured results of the microwave intensity in the vicinity of the central antenna for the system with 60 small scatterers (radius 2.55 mm). The areas in the immediate vicinity of the central antenna as well as of the scatterer positions were not accessible in the experiment and were therefore coloured black in the plots. Each pixel represents an area of 5×5 mm in the waveguide. For a meaningful comparison, the numerical results, which are available on a very dense mesh underlying our finite-element simulations, have been mapped to the same pixelated positions as in the experiment. **b,** Corresponding results for the system with 60 mixed size scatterers (radii 2.55 mm and 11 mm).

Supplementary section 5 – Global absorption effects

Our random anti-laser is characterised by a disordered medium with an absorptive element embedded. However, not only the localised absorber contributes to the attenuation of the injected signal but also the effect of globally distributed loss. As a result, we have two different absorption mechanisms in our system: on the one hand we have a controllable localised absorber represented by the central absorbing antenna, and on the other hand there is the ubiquitous global absorption induced, e.g., by absorption in the metallic top and bottom waveguide plates or by the escape through the small holes in the top plate. While this global absorption cannot be controlled as efficiently as our local absorbing antenna, it still plays a role that we discuss in this section. As an estimate for the absorption of the bare waveguide (with holes), we measured the mean transmission through it. Averaging over all modes and frequencies in the range from 6.55 GHz to 7.35 GHz, we found that 85.9% of the injected intensity was transmitted.

The effect of the localised absorbing antenna compared to global absorption effects can be nicely seen in Fig. S5.1. There we show the minimal eigenvalue $|\lambda_{\min}|^2$ of the scattering matrix as a function of the microwave frequency for two different scatterer configurations. In the first case, where we use a set of 60 small scatterers (radius 2.55 mm), the squared absolute value of the minimal S-matrix eigenvalue without absorbing antenna is about $|\lambda_{\min}|^2 \approx 0.74$ (averaged over the range from 6.55 GHz to 7.35 GHz). Only if the absorbing antenna in the middle of the scattering region is implemented, we find minimal eigenvalues that are strongly reduced for certain frequencies (e.g., around 7.1 GHz in Fig. S5.1a). In the second case, however, when we use 60 scatterers of mixed sizes (radii 2.55 mm and 11 mm), the minimal eigenvalues become relatively small even without the absorbing antenna, as for example in the region around 6.6 GHz in Fig. S5.1b. Nevertheless, the absorbing antenna improves the absorption efficiency also in the case of mixed scatterer sizes, in particular at frequency ranges where the minimal eigenvalue without absorbing antenna is rather large, as can be seen at about 7.35 GHz in Fig. S5.1b. For the configuration which also contains the large scatterers (radius 11 mm), scattering is more efficient and the longest achievable dwell times inside the scattering region become much larger as compared to the case where only small scatterers are used. As a result, also the effect of the global absorption becomes more pronounced, especially for those states that remain strongly trapped in a spatial region that has no overlap with the central antenna.

In strongly scattering systems one can also find CPA states which are mainly induced by global absorption and where the localised absorbing antenna plays only a subordinate role. As an example, we investigate the occurrence of CPA states in a system consisting of 75 mixed size scatterers (radii 2.55 mm and 11 mm) in Fig. S5.2. In the left panel of Fig. S5.2a we display the minimal eigenvalue of the S-matrix together with the reflection signal for injection into the central antenna. The antenna length of 6 mm was chosen by the fact that this length produced the deepest reflection minimum in the studied frequency interval. We first notice that, compared to the results for the system with 60 small scatterers (see Fig. S5.1a and Fig. S6), the resonances of the minimal S-matrix eigenvalue are noticeably sharper when also the larger scatterers are included in the scattering system. In addition to a local S-matrix eigenvalue minimum close to the position of the minimal reflection signal, we also find several other resonant eigenvalue minima at frequency values where the coupling of the central antenna to the system is much weaker and not resonant at all.

This behaviour thus points to the presence of CPA states in the system whose absorption is not dominated by the central antenna, but by the global absorption in the waveguide (a situation that occurs, e.g., when field modes are strongly trapped in spatial regions that are remote from the antenna). Nevertheless, we can inject the corresponding CPA eigenstates into the system and find an almost perfect absorption (see blue curve in Fig. S5.2a for the CPA state around 6.725 GHz). In the same way as already demonstrated for the CPA state presented in Fig. 2 of the main text, the ratio between outgoing and incoming microwave intensity strongly depends on the signal frequency and, remarkably, also on the absorption by the central antenna. While the antenna is not the dominant source of loss here, the small but non-zero field overlap with it can still be used to tune a CPA to and away from the point of maximal absorption. Moreover, the absorption efficiency of the CPA state is also very sensitive to detunings in the optimal IQ-modulator amplitude and phase settings (see Fig. S5.2b).

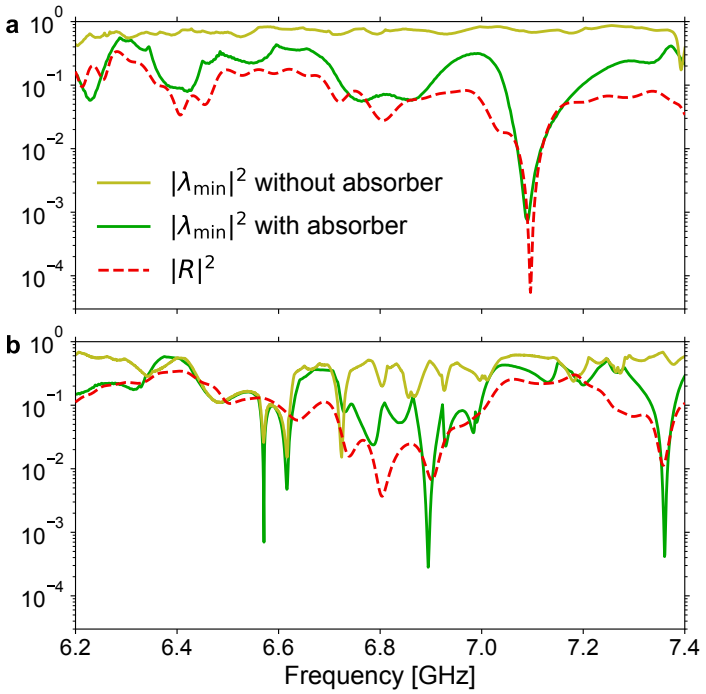

Supplementary figure S5.1: Influence of the localised absorbing antenna compared to global absorption effects. a, Minimal S-matrix eigenvalue $|\lambda_{\min}|^2$ for a system with 60 small scatterers (radius 2.55 mm) both for the cases without and with the central absorbing antenna (length 7 mm) in place, compared to the reflection signal $|R|^2$ at injection into the central antenna. **b,** Corresponding plot for a system with 60 scatterers of mixed sizes (radii 2.55 mm and 11 mm).

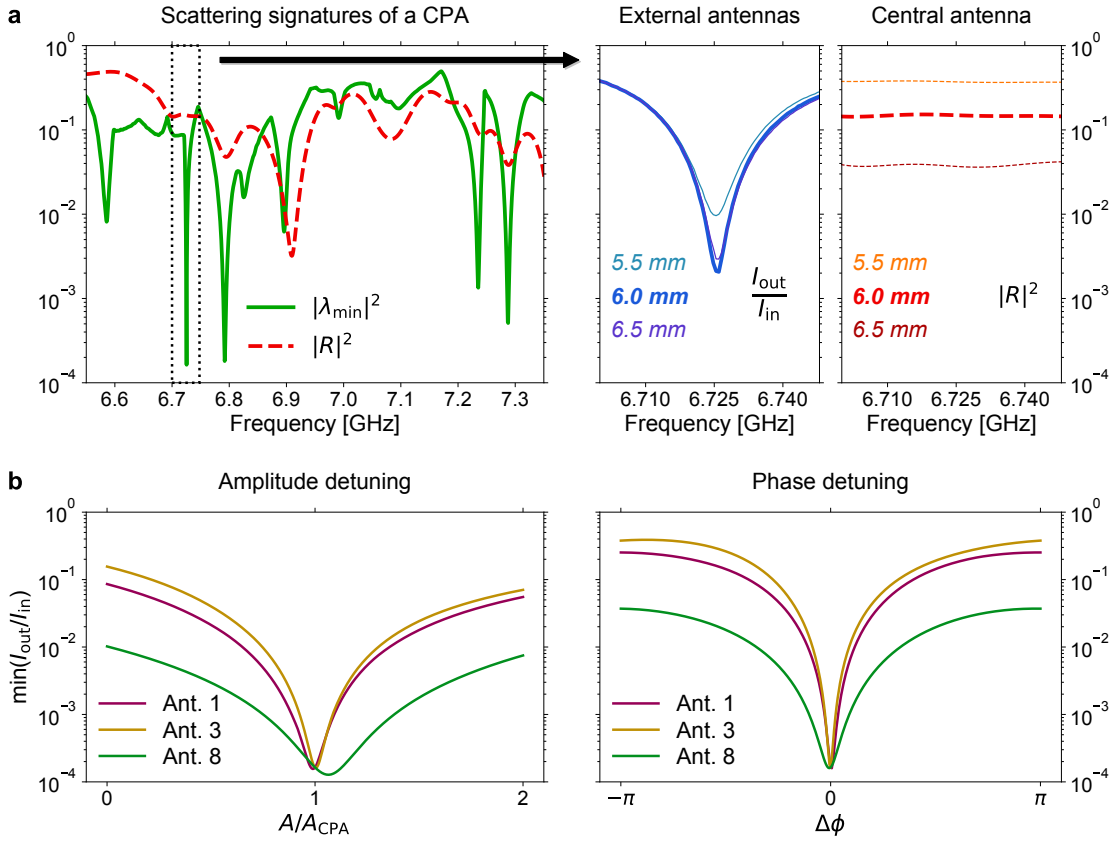

Supplementary figure S5.2: CPA induced by global absorption. a, Minimal S-matrix eigenvalue $|\lambda_{\min}|^2$ compared to the reflection signal $|R|^2$ at an absorbing antenna of length 6 mm for a system consisting of 75 mixed size scatterers (radii 2.55 mm and 11 mm). The panels on the right show the ratio between the outgoing and incoming intensity $I_{\text{out}}/I_{\text{in}}$ for the CPA state corresponding to the eigenvalue minimum around 6.725 GHz, as well as the reflection coefficient $|R|^2$ at the central antenna, each determined for different lengths of the central antenna. **b,** In analogy to the procedure applied in Fig. 2b of the main text, we vary the amplitude A and relative phase ϕ at individual input antennas to show the sensitivity of the CPA state to detunings in individual IQ-modulators. The results presented in **b** were generated by linear superposition of the data from the S-matrix measurement whereas the blue curve in **a** represents a direct measurement of the injected CPA state.

Supplementary section 6 – Investigation of the minimal eigenvalue of the scattering matrix

The principle behind our approach to find CPA states is to identify S-matrix eigenstates corresponding to a zero eigenvalue. Therefore, the first step in the realisation of a CPA is the determination of the S-matrix and the evaluation of its eigenvalues. Fig. S6 depicts the minimal S-matrix eigenvalue as a function of the signal frequency together with the ratio between outgoing and incoming intensity of a CPA state as well as the reflection signal from injection at the absorbing antenna for a system configuration with 60 small scatterers (radius 2.55 mm). In the frequency range around 7.1 GHz, the reflection signal from injection at the absorbing antenna has a distinct minimum, which means that the antenna is particularly well coupled to the system at this signal frequency. Correspondingly, also the minimal S-matrix eigenvalue becomes very small near that frequency. However, the minima of the S-matrix eigenvalue and the reflection signal do not coincide at the exact same frequency but are slightly shifted against each other. This frequency shift is a result of global absorption effects, which are also the reason for the difference between the

CPA state and the time-reversed output state from injection at the central antenna. Moreover, also the minima of the minimal S-matrix eigenvalue and the intensity ratio of the CPA state are shifted against each other. The reason for this effect is mainly that the eigenstates cannot be perfectly injected due to the finite step size of the IQ-modulator settings, which limits the injection accuracy of a specific state. The injected state is therefore not exactly the respective eigenstate and features its optimal absorption efficiency at a slightly shifted frequency compared to the previously determined S-matrix eigenvalue. The right panel in Fig. S6 displays the minimal S-matrix eigenvalue determined for different absorbing antenna lengths. It turns out that both for shorter and longer absorbing antennas the absorption efficiency is significantly decreased compared to the results for the optimal CPA antenna length of 7 mm.

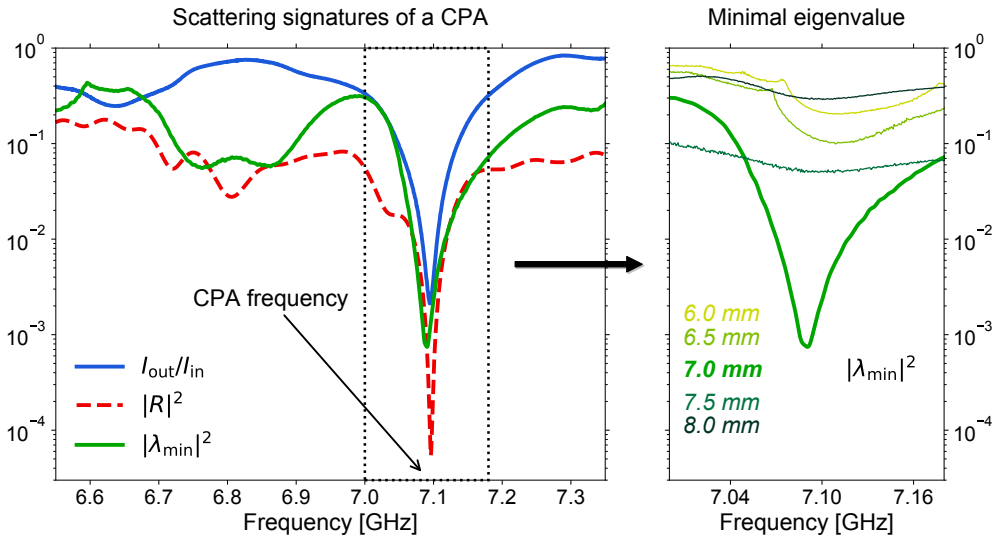

Supplementary figure S6: Analysis of the minimal S-matrix eigenvalue. The plot on the left depicts the ratio between the outgoing and incoming intensity I_{out}/I_{in} of a CPA state for the system with 60 small scatterers (radius 2.55 mm) together with the reflection signal $|R|^2$ measured at the absorbing antenna (for injection at the central antenna) as a function of the signal frequency. While these two quantities are the same as in Fig. 2a of the main text, we additionally include here the minimal S-matrix eigenvalue $|\lambda_{min}|^2$ for the same system configuration (see green curve). The panel on the right shows this minimal S-matrix eigenvalue determined for different absorbing antenna lengths. Most importantly, we find that an antenna length of 7 mm is ideal for reaching a minimum also in this eigenvalue (not just in the reflection signal).

Supplementary section 7 – Time-reversal symmetry

Coherent perfect absorption is the time-reversed process of lasing at threshold. This means that one can in principle build a CPA from a laser by replacing its gain medium by a medium with the same amount of loss. This structure would then perfectly absorb the time-reversed counterpart of the signal emitted by the laser at its first threshold. In our system, this conceptual understanding can directly be implemented by injecting a signal with the CPA frequency at the critically coupled central antenna. The resulting microwave signal leaving the waveguide should then represent the time-reversed version of the CPA input state. In Fig. S7 we show this time-reversed state explicitly, together with the corresponding CPA input state for the system with 60 small scatterers (radius 2.55 mm). Featuring a correlation of about 99%, the time-reverse of the outgoing signal for injection at the central antenna looks

very similar to the CPA state, which we found independently for the same scatterer configuration using the approach outlined in the main text. Small deviations are again due to global absorption effects, which cannot be converted into the respective gain, such that the CPA state is not exactly the time-reversed counterpart of the measured signal for injection at the central antenna. In addition, the basis for the determination of the CPA states are the S-matrix measurements, which constitute a weak but non-vanishing perturbation of the system when the movable antenna dips into the waveguide. Although the scattering effect of the movable antenna is verifiably small, it is still sufficient – along with other experimental imperfections like the back-reflection at the external antennas – to cause noticeable deviations.

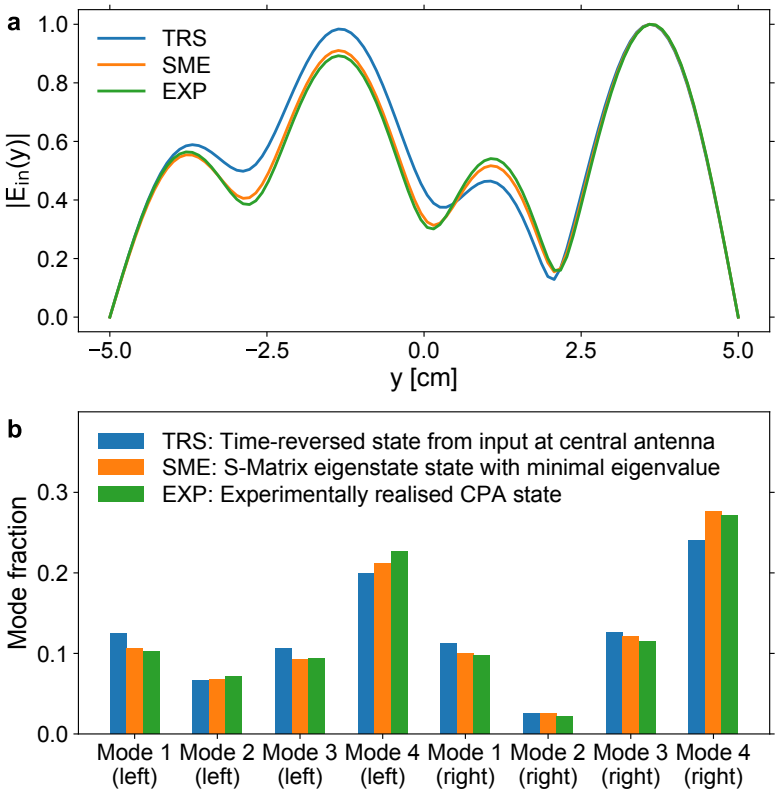

Supplementary figure S7: Time-reversal symmetry analysis of a CPA state. a, Comparison of the normalised incoming microwave fields E_{in} along the waveguide width (y-direction) at one waveguide end for a time-reversed state (TRS) created experimentally with input at the central antenna and a CPA state for a system with 60 small scatterers (radius 2.55 mm). The S-matrix eigenstate (SME) is the eigenstate corresponding to the minimal eigenvalue of the experimentally measured S-matrix and the experimentally injected CPA state (EXP) is the actually realised SME (including all experimental imperfections in addition to those already present in the scattering matrix alone). **b,** Analysis of the three states from **a** in the mode domain. The bars illustrate the fraction of the respective mode in the incoming signal.

In our numerical simulations, where we neglect global absorption, we calculate the time-reversed CPA states in the following way: we place an emitting point source in the scatterer representing the antenna (which serves as a good approximation since the scatterer is small) and turn the scatterer's loss into the corresponding amount of gain. For both configurations considered in the main manuscript, the resulting correlation between the intensities of the CPA state and the time-reversed state is unity up to 10^{-14}, thus proving the time-reversal symmetry between a CPA and a laser operating at its threshold.

In the context of time-reversal one may wonder if a true time-reversal of the entire experiment not also requires to turn all of the experiment's absorption effects into time-reversed gain effects. Upon time-reversal the absorbers placed at the outer ends of the waveguide would then, e.g., emit radiation towards the scattering region, insertion losses would turn into insertion gains, etc. Apart from the fact that such a full time-reversal is of course cumbersome to implement, we also need to stress here that we are interested only in the time-reversal of the wave scattering problem that unfolds in the region between the four external antennas on either side of the waveguide (see Fig. 1 in the main text).

To restrict ourselves explicitly to this sub-part of the system we measured the scattering matrices, the injected CPA states and the ejected states originating in the central antenna all in the space between the scattering region and the external antennas. Also the IQ-modulator settings necessary to inject a CPA state were determined from measurements performed at these same positions. Therefore, all the attenuation effects between the vector network analyser and the external antennas reaching into the waveguide are already taken into account for the generation of our CPA states. At the same time, we need to stress here that the eight external antennas as well as that used for scanning the field and for evaluating the scattering matrix are all weakly coupled to the waveguide (in contrast to the central absorbing antenna, which is strongly coupled). This means that these external antennas do not lead to any significant scattering contributions that would have to be considered in the time-reversal. Consider, for this purpose, that the reflection matrix elements in the scattering matrix of the empty waveguide are all very strongly reduced (see Fig. S2, left panel) although for their measurement the external antennas were present in the waveguide. Correspondingly, also when we place the disorder inside the central scattering region all waves that emanate from this disordered part of the waveguide will never return back there (even in the presence of the external antennas).

If we now apply these considerations to the time-reversal of the CPA state, we first notice that the CPA state has only incoming flux components in the two regions where we measure the scattering matrix. Correspondingly, the time-reversed state we aim to create has only outgoing flux components in these external regions. As mentioned above, such purely outward-flowing wave fields are those emanating from the central scattering region (i.e. from the central antenna if we neglect that the global loss cannot be time-reversed). To generate the time-reversed CPA-state one could, in principle, also include the time-reversed external absorbers and antennas. Since waves that would then be emitted by these elements must, however, produce no inward-flowing contribution it is clear that the time-reversal of the external absorbers and of the external antennas must fully cancel each other at the CPA frequency even before entering the near-field of the disordered scattering region. Apart from the fact that one would thus not observe any effect in the sub-part of the system we are interested in, such an extended time-reversal operation would also be unnecessarily complicated in practice as several more injection ports would have to be controlled.

Supplementary section 8 – Determination of mean free paths

To quantify the scattering properties of a disordered system, two very useful length scales have been proposed in scattering theory. The macroscopic transport properties are well characterised by the transport mean free path l_t, which measures the length at which the direction of an incoming photon is entirely randomised. On a more microscopic level, the scattering mean free path l_s measures the average distance between two scattering events, which thus characterises the scattering strength.

To determine the transport mean free path for the disordered waveguides we work with, we first calculate the scattering matrices of 1000 random configurations with the same density and size distribution of scatterers as in the experiment. We also take the scattering effect of the central antenna into account by including the scatterer in our simulations that represents the central antenna. To avoid that we also include the absorption effect of this scatterer, we just work with the real part of its refractive index. Randomly concatenating many of these scattering matrices then leads to a localisation of the wave, in which the average transmission decays exponentially, i.e., $\langle \ln T \rangle \approx -L/\xi$, with $T = \mathrm{Tr}(t^\dagger t)/N$, where t is the transmission matrix and N is the number of modes. Therefore, averaging for each length of the concatenated waveguides the logarithm of T over 1000 random configurations and fitting $\langle \ln T \rangle$ to $-L/\xi$ yields the localisation length ξ. For quasi-1D systems like ours, ξ is related to the transport mean free path via $\xi \approx N\, l_t$. Based on this analysis, we find that the transport mean free path in the configuration with small (mixed) scatterers is $l_t \approx 1.3\ \mathrm{m}$ ($l_t \approx 0.2\ \mathrm{m}$), which is about twice as large (three times as small) as the length of our scattering region (0.6 m). We checked these results also by an independently performed fitting procedure based on the Ohmic behaviour in the diffusive regime.

In a next step, we also evaluate the scattering mean free path, which is related to the transport mean free path by $l_t = l_s/(1-g)$. Since the anisotropy parameter g is, however, not directly accessible to us, we extract the scattering mean free path directly from our numerical simulations. To do so, we split the disordered waveguide into shorter subsections with a proportionally smaller number of included scatterers. Choosing the subsections such that the wave still propagates ballistically in them (transmission is still above 90%), we study the decrease of the diagonal transmission elements $T_{nn} = |t_{nn}|^2$ to quantify how much an incoming mode is scattered into other modes. Since the decrease of the diagonal transmission elements in the ballistic regime is linear, we average T_{nn} for each mode over 1000 random configurations and fit the following expression, $\langle T_{nn} \rangle \approx 1 - L/l_{s,n}$, to obtain the mode-specific scattering mean free paths $l_{s,n}$. Further averaging over all these modes then yields the average scattering mean free path $l_s \approx 1.3\ \mathrm{m}$ ($l_s \approx 0.08\ \mathrm{m}$) in the case of the configuration with small (mixed) scatterers, which is about twice as large (seven to eight times as small) as the length of our scattering region (0.6 m).

As can be seen from the above results, both mean free path values are equivalent $l_t \approx l_s$ for the configuration with small scatterers and comparable to the length of the scattering region. Due to the sub-wavelength size of the small scatterers, s-wave scattering is dominant in this case, i.e., the scattering cross section is the same in all angles (corresponding to an anisotropy parameter $g = 0$). However, in the more strongly scattering configuration with mixed scatterers forward-scattering is more pronounced than backward-scattering which results in $g > 0$ and thus $l_t > l_s$, where we specifically find that $l_t \approx 2.5\, l_s$.

Supplementary section 9 – Observability of CPA states

The reason why we always observe a CPA state in our experiment (for all of the different disorder configurations that we choose at random) and why, in fact, we can be sure that we don't have to perform any disorder-engineering to reach a CPA point is explained as follows: in an open disordered system without any loss or gain the poles and zeros of the scattering matrix are symmetrically distributed with respect to the real axis. Correspondingly, the number of poles and of zeros per (real) frequency interval is the same and on average given by the Weyl law that provides the average density of states just based on the area of the scattering region. According to this Weyl estimate we can expect (independently of the disorder configuration chosen) that around 30 poles and zeros fall within the frequency interval between 6.55 GHz and 7.35 GHz that we scan in our experiment. When adding the absorption antenna to the scattering region all of these zeros move downwards to the real axis and will hit it eventually to realise a CPA condition within the frequency interval we monitor in the experiment.

In line with these arguments really no disorder engineering is necessary: as long as the studied frequency interval is considerably larger than the mean level spacing, a CPA can always be realised – provided, of course, that also the absorption in the system can be made large enough to drag S-matrix zeros all the way down to the real axis. Another special case we can think of where a CPA condition may not be found is when the considered frequency interval coincides with a band gap of the medium such as in hyper-uniform disordered media. But these are of course purposefully engineered systems that will not occur for the standard random configurations out of the box that we are considering here.

In all the cases presented in this manuscript the scatterer positions were chosen randomly without any adjustments a posteriori. A restriction we applied was to place the scatterers not too close to the antenna and to keep the antenna approximately in the centre of the scattering region. From the measurements we performed, we also found that critical coupling is harder to achieve when the position of the antenna is close to the boundary of the scattering region or close to the boundary of the waveguide, which we therefore avoided.

Regarding the widths of the scattering layers on the left and right of the absorbing antenna we can make the following statements: (i) For very short scattering layers or for very weak scattering in the disorder, much loss is needed to move the S-matrix zeros down to the real axis. In this way a restriction on the maximally achievable loss value of the central absorber results in a minimum length of the scattering layer or a minimum amount of scattering to reach a CPA point. (ii) For very thick scattering layers or for very strong scattering, on the contrary, the CPA resonances may spectrally be very sharp such that it is crucial not to miss them in the frequency scanning. The loss values to reach a CPA point are, however, very small in this case.